Exploiting Aggregation and Segregation of Representations for Domain Adaptive Human Pose Estimation

Qucheng Peng¹, Ce Zheng², Zhengming Ding³, Pu Wang⁴, and Chen Chen¹ Center for Research in Computer Vision, University of Central Florida, Orlando, USA

²Robotics Institute, Carnegie Mellon University, Pittsburgh, USA

³Department of Computer Science, Tulane University, New Orleans, USA

⁴University of North Carolina at Charlotte, Charlotte, USA

{qucheng.peng, chen.chen}@ucf.edu

Abstract—Human pose estimation (HPE) has received increasing attention recently due to its wide application in motion analysis, virtual reality, healthcare, etc. However, it suffers from the lack of labeled diverse real-world datasets due to the time- and labor-intensive annotation. To cope with the label deficiency issue, one common solution is to train the HPE models with easily available synthetic datasets (source) and apply them to real-world data (target) through domain adaptation (DA). Unfortunately, prevailing domain adaptation techniques within the HPE domain remain predominantly fixated on effecting alignment and aggregation between source and target features, often sidestepping the crucial task of excluding domain-specific representations. To rectify this, we introduce a novel framework that capitalizes on both representation aggregation and segregation for domain adaptive human pose estimation. Within this framework, we address the network architecture aspect by disentangling representations into distinct domain-invariant and domain-specific components, facilitating aggregation of domain-invariant features while simultaneously segregating domain-specific ones. Moreover, we tackle the discrepancy measurement facet by delving into various keypoint relationships and applying separate aggregation or segregation mechanisms to enhance alignment. Extensive experiments on various benchmarks, e.g., Human3.6M, LSP, H3D, and FreiHand, show that our method consistently achieves stateof-the-art performance. The project is available at https: //github.com/davidpengucf/EPIC.

I. INTRODUCTION

2D human pose estimation (HPE) from monocular images is an important task in computer vision and has witnessed great success thanks to the advancement of deep neural networks. As with any task, the training of deep learning models necessitates vast amounts of labeled data [4], [15], [23], [54]. For the HPE task, collecting real-world datasets with diverse appearances and poses and generating groundtruth annotations are time- and labor-intensive. On the contrary, synthetic datasets with annotations are much cheaper and easier to acquire due to the development of computer graphics and game engines. Therefore, one can essentially generate an (infinite) number of labeled synthetic samples to train HPE models. However, models trained on synthetic data may not generalize well on real-world data in terms of the data distribution discrepancy. In this case, domain adaptation (DA) plays a key role in generalizing the synthetic data (source) trained models to real-world (target) data [2], [57], [28], [50], [31], [55].

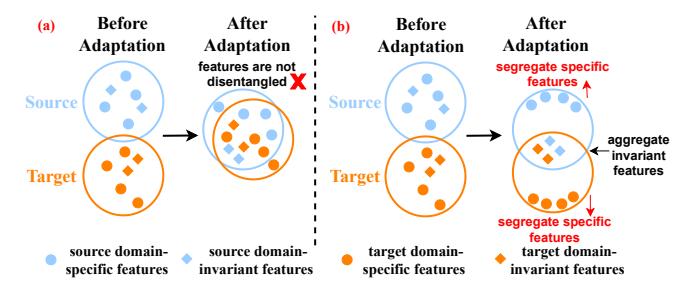


Fig. 1: Comparison of (a) previous works and (b) our objective. Previous works align source and target directly, which may result in suboptimal performances due to the mixing of diverse features. Our objective aggregates domain-invariant features and segregates domain-specific features simultaneously to craft a good regressor in the target domain.

In the context of DA, learned representations encompass two vital components: domain-invariant and domain-specific elements [36], [10]. This dichotomy is also observed in DA for HPE [16], [17], [12]. **Domain-invariant features**, such as kinematic attributes within human poses, enhance knowledge transfer across domains, while domain-specific features like body scale and viewpoint impede effective cross-domain learning. Conventional approaches [26], [21], [16], [17], [19] in DA for HPE often amalgamate and align source and target features without discerning these intrinsic components (see Fig. 1a). These approaches often result in suboptimal performances due to the mixing of diverse features. To disentangle the mixed features better, we emphasize the incorporation of source-invariant and target-invariant features in the adaptation process, while preserving target-specific characteristics and reducing the impact of source-specific attributes. As depicted in Fig. 1b, our approach aims to achieve this objective by disentangling representations from both the source and target domains into domain-invariant and domain-specific components. We prioritize target pose estimation by aggregating domain-invariant attributes, thus fostering positive knowledge transfer from source to target. Furthermore, we segregate source-specific and target-specific features, thereby shielding target-specific representations and mitigating any adverse effects stemming from source-specific representations.

While our previous discussion viewed aggregation and

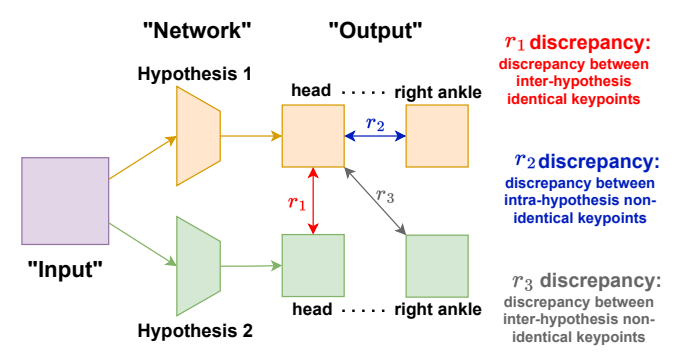


Fig. 2: Hypothesis discrepancy based on multiple relations. Apart from the r_1 discrepancy (marked red) that is considered by existing methods, we enhance identical hypotheses consistency by r_2 discrepancy (marked blue) and non-identical hypotheses discrimination by r_3 discrepancy (marked gray).

segregation from a network perspective, this is insufficient to tackle the complexities inherent in human pose estimation, whose output comprises multiple keypoints such as head, hips, and ankles (see Fig. 2), each with distinct attributes. For heatmaps corresponding to the same keypoint (keypointwise) or generated by the same hypothesis (hypothesis-wise), it is anticipated that they exhibit similarity in their representations through specific aggregation strategies, and conversely, dissimilarity should be appropriately measured through specific segregation strategies. To fulfill this need, we introduce a novel discrepancy measurement, depicted in Fig. 2. This measurement takes into account three distinct types of relations between pairs of estimation outputs: r_1 relations involving inter-hypothesis identical keypoints, r_2 relations encompassing intra-hypothesis non-identical keypoints, and r_3 relations associated with inter-hypothesis non-identical keypoints. Prevailing methodologies [16], [19], [17], [12] predominantly focus on aggregating r_1 relations exclusively. In contrast, our approach transcends these limitations. It not only aggregates r_1 relations but also incorporates aggregation of r_2 relations while simultaneously segregating r_3 relations. Detailed explanations are provided in Sec. III-D. The primary contributions of this paper can be summarized as follows:

- We introduce a novel framework that disentangles features into domain-invariant and domain-specific components, conducting aggregation and segregation on them separately to reduce the domain gap.
- We propose a new hypothesis discrepancy measurement for human pose estimation, aggregating the intrahypothesis non-identical discrepancy and segregating the inter-hypothesis non-identical discrepancy.
- We conduct comprehensive experiments on several domain-adaptive HPE benchmarks and the results show that our method outperforms the state-of-the-art approaches by a considerable margin.

II. RELATED WORK

A. Human Pose Estimation

In this paper, we focus on domain adaptation in 2D HPE, which can be divided into regression methods and heatmap-based methods. Regression methods directly output keypoints coordinates. Starting from [43], deep neural networks are applied in HPE. [39] introduces a structure-aware regression method that uses bone-based representations. [22] combines vision transformers [6], while [35] proposes a fully end-to-end method trained in one single stage. For heatmap-based methods, the networks first obtain heatmaps constructed by putting 2D Gaussian kernels on the potential keypoints, then convert heatmaps to coordinates. [3] uses global and refine nets to improve performance. [47] proposes Simple Baselines to simplify the network structures. [38] fully utilizes all the features at different scales. Besides, some work tends to improve the quality of heatmaps, like [52] that extends Gaussian to second order in heatmaps and [25] that proposes scale-adaptive heatmaps. In our model, we follow previous works [16], [19] to use the heatmap-based approach and apply Simple Baselines as the backbone.

B. Domain Adaptation

There are two kinds of approaches for domain adaptive image classification, i.e., statistics-matching and adversarialbased methods. Statistics-matching methods measure the discrepancy between source and target, and then minimize the discrepancy. To name a few, [24], [49] uses maximum mean discrepancy [27], [44] applies deep domain confusion and [37], [32] utilizes correlation relation. [46] uses this paradigm for heterogeneous domain adaptation, and [5] jointly makes clustering and discrimination for alignment. Adversarialbased methods are inspired by generative adversarial networks [8], which play a min-max game for two domains. For example, [7] builds confusion domains. [34] tackles with the game of two classifiers. [51] shows that learning larger feature norms matter and [41] reveals that discriminative clustering can benefit the adaptation. Our method applies the adversarial structure and also adopts the maximum mean discrepancy technique from statistics-matching.

C. Domain Adaptive Human Pose Estimation

Domain-adaptive HPE methods can be divided into two categories. One is the shared structure, in which the networks of source pretrain and target adaptation share weights. CC-SSL [26] uses one network trained in an end-to-end fashion. RegDA [16] applies one shared feature extractor and two separate regressors. TransPar [12] adopts a similar structure but focuses on transferable parameters. The other adopts an unshared structure, where the pretrain and adaptation form a teacher-student paradigm. To name a few, MDAM [21] tackles this structure, together with a novel pseudo-label strategy. UniFrame [19] modifies the classic Mean-Teacher [42] model, combining with style transfer [14]. MarsDA [17] edits RegDA in a teacher-student manner [29]. [30], [33] discuss a specific setting called "Source-free", which is different from others, so we do not compare to them.

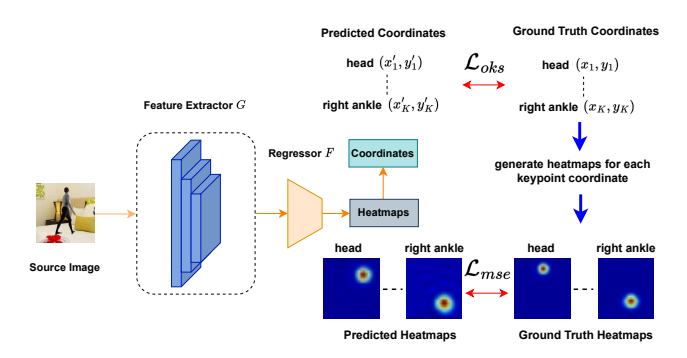


Fig. 3: Pipeline of the supervised 2D HPE, and the **source-pretraining process** of our method. After passing feature extractor G and regressor F, each source image turns to be K heatmaps corresponding to K keypoints. After certain transforms, K 2D keypoints are obtained. We use these heatmaps and coordinates to compute \mathcal{L}_{mse} and \mathcal{L}_{oks} .

The shared structure has fewer parameters and is easy to converge, but the shared weights suffer from domain shifts. The unshared one can resist domain shifts by separate networks, but the convergence speed is slower. Our method adopts the shared structure and uses intermediate representations to combat domain shifts.

III. METHODOLOGY

A. Problem Statement

In 2D HPE, we have a labeled pose dataset $\mathcal{D} = \{(x_i, y_i)\}$, where $x_i \in \mathbb{R}^{C \times H \times W}$ is the image and $y_i \in \mathbb{R}^{K \times 2}$ is the corresponding keypoint coordinates. Here H and W are the height and width of the image and C is the number of channels. Besides, K is the number of keypoints. For the sake of smoother training, most existing 2D methods use heatmaps $M_i \in \mathbb{R}^{K \times H' \times W'}$ to represent coordinates in a spatial way during supervised learning, where H' and W' are the height and width of heatmaps. In the inference stage, well-trained supervised models output heatmaps that predict the probability of joints occurring at each pixel. For each heatmap, the pixel with the highest probability is treated as the predicted joint's location. We define the transform from heatmaps to coordinates as $T: \mathbb{R}^{K \times H' \times W'} \to \mathbb{R}^{K \times 2}$, and the inverse transform from coordinates to heatmaps as $T^{-1}: \mathbb{R}^{K \times 2} \to \mathbb{R}^{K \times H' \times W'}$.

In the domain adaptive HPE setting, we have a source domain dataset $\mathcal{S} = \{(x_i^s, y_i^s)\}_{i=1}^{n_s}$ with n_s labeled pose samples. $x_i^s \in \mathbb{R}^{C \times H \times W}$ is the source image and $y_i^s \in \mathbb{R}^{K \times 2}$ is the corresponding pose annotation. Besides, there exists a target domain dataset $\mathcal{T} = \{x_i^t\}_{i=1}^{n_t}$ that includes n_t unlabeled pose samples. The source and target domains share the same label space but lie in different distributions. Our goal is to use the labeled source dataset and unlabeled target dataset to obtain a model that achieves high performance on the target dataset.

B. Source Domain Pretraining

For DA in HPE, labeled source data are used for model pretraining as the first step. Same as most existing domain

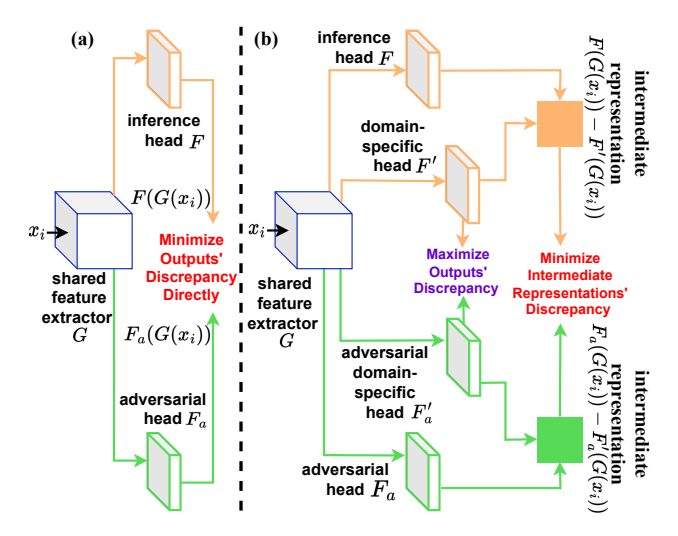


Fig. 4: Comparisons between (a) conventional structure and (b) our proposed Intermediate Domain Framework (IDF). Details are provided in Section III-C. (Best viewed in color and zoom in)

adaptive pose estimation methods [26], [21], [16], [19], the network is composed of a feature extractor G (such as ResNet backbone) and a pose regressor F as shown in Fig. 3. Here we first adopt the coordinate loss called Objective Keypoint Similarity (OKS) loss [35], which can be represented as:

$$\mathcal{L}_{oks}(\hat{y}, y) = \sum_{i=1}^{K} \exp\left(\frac{-\|\hat{y}_i - y_i\|_{\ell_2}}{2sk_i}\right), \tag{1}$$

where \hat{y} is the predicted coordinate and y is the ground-truth coordinate. $\|\cdot\|_{\ell_2}$ is the Euclidean distance between the prediction and ground truth of keypoint i, and k_i is a keypoint constant that controls falloff. s is the area of the input image. During the pretraining, we combine the heatmap-based loss (MSE loss) and the coordinate-based loss (OKS loss) as the overall loss:

$$\mathcal{L}_{pretrain} = \mathbb{E}_{(x_i^s, y_i^s) \in \mathcal{S}} \mathcal{L}_{mse}(F(G(x_i^s)), T^{-1}(y_i^s)) + \mathbb{E}_{(x_i^s, y_i^s) \in \mathcal{S}} \mathcal{L}_{oks}(T(F(G(x_i^s))), y_i^s),$$
(2)

where \mathcal{L}_{mse} denotes the Mean Squared Error (MSE) loss between the heatmap representations of prediction and ground truth. Though the argmax operation in T^{-1} is non-differentiable, we use a differentiable *soft-argmax* proposed in [40].

C. Network Structure for Domain Adaption

In previous works [16], [12], [17], the conventional network structure consists of one shared feature extractor G and two regression heads: the inference head F and the adversarial head F_a , as depicted in Fig. 4(a). The discrepancy measurement between these two heads is defined as $\|F(G(x_i)) - F_a(G(x_i))\|_{\ell_2}$ for a given input x_i . As mentioned earlier in the introduction section, domain-specific characteristics persist in both heads, which hinders the aggregation procedure of their outputs.

To address this issue, we expand the two heads to two branches, as illustrated in Fig. 4(b). The inference branch (orange color) includes the inference head F and the domain-specific head F'. Similarly, the adversarial branch (green color) contains the adversarial head F_a and the adversarial domain-specific head F'_a . The purpose of F' and F'_a is to disentangle and extract domain-specific representations, denoted as $F'(G(x_i))$ and $F'_a(G(x_i))$. Enlarging the discrepancy between these representations is beneficial for learning invariant knowledge [11].

By utilizing domain-specific representations, we obtain intermediate representations as $F(G(x_i)) - F'(G(x_i))$ (the orange square in Fig. 4b) and $F_a(G(x_i)) - F'_a(G(x_i))$ (the green square in Fig. 4b). These representations serve as bridges between the two branches, and minimizing their discrepancy helps to reduce the difficulty of knowledge transfer. In conclusion, the discrepancy measurement \mathcal{L}_{dl} between the two branches contains the aggregation of intermediate representations \mathcal{L}_{inter} and the segregation of specific representations \mathcal{L}_{spec} :

$$\mathcal{L}_{dl}(x_i) = \mathcal{L}_{inter}(x_i) - \mathcal{L}_{spec}(x_i), \tag{3}$$

where the first term corresponds to the minimization of intermediate representations' discrepancy, and the second indicates the maximization of specific representations' discrepancy. Further details on how we compute these two terms separately are included in Sec. III-D.

D. Discrepancy Measurement

In this section, we propose a new discrepancy measurement that is designed for the pose estimation problem, especially for the min-max game. Hypothesis disparity frameworks in domain adaptation are inspired by Maximum Classifier Discrepancy (MCD) [34], [48], which maximizes and minimizes hypothesis discrepancy to form the min-max game. For some existing methods like [16], [17], [12], MSE or KL divergence is applied as their discrepancy losses, but these losses are not enough for DA in HPE tasks. For HPE, the outputs of the regressors are much more complex than classification outputs. The outputs of classification are just digits, but the regressors generate one heatmap for each keypoint, so simple MSE or KL divergence between heatmaps from different hypotheses cannot show the hypothesis disparity completely. Therefore, we introduce Maximum Mean Discrepancy (MMD) [9], which estimates the distance between two hypotheses based on observed samples:

$$D_{\mathcal{H}}(p,q) = \mathcal{MMD}(h_i, h_j) = \|\phi(h_i) - \phi(h_j)\|_{\mathcal{H}}^2, \quad (4)$$

where h_i and h_j are distinctive outputs and $\phi(\cdot)$ is a map that projects them to the Reproducing Kernel Hilbert Space (RKHS) and is related to a Gaussian kernel κ as $\kappa(x_1, x_2) = \langle \phi(x_1), \phi(x_2) \rangle$, where $\langle \cdot, \cdot \rangle$ denotes the vector inner product. p and q are different hypotheses. We generalize MMD to the pose estimation, assuming $\mathbf{H_i} = F(G(x_i)) = \begin{bmatrix} h_{i,1}, h_{i,2}, \cdots, h_{i,K} \end{bmatrix}^{\mathsf{T}}$, then MMD between two keypoints is defined as:

$$\mathcal{MMD}_{keypoint}(h_{i,m}, h_{j,n}) = \left\| \phi(h_{i,m}) - \phi(h_{j,n}) \right\|_{\mathcal{U}}^{2}, (5)$$

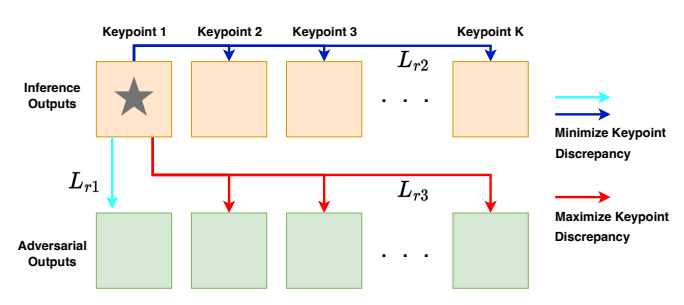


Fig. 5: Proposed discrepancy loss. Here the keypoint with a star is used for illustration. Keypoints connected with a cyan arrow are inter-hypothesis identical (r_1 relation). L_{r1} in Eq. (7) is used to describe their discrepancy. Keypoints marked with blue arrows are intra-hypothesis non-identical (r_2 relation) and represented with L_{r2} in Eq. (7). Keypoints linked with red arrows are inter-hypothesis non-identical (r_3 relation) computed by L_{r3} in Eq. (7).

where i and j represent different outputs, while m and n correspond to distinctive keypoints.

Moreover, the relations between the two hypothesis outputs are more complicated. For probabilistic outputs, we just deal with the digits at the same location one by one with ℓ_1 distance. But for pose estimation, three types of relations matter as shown in Fig. 5. One is inter-hypothesis identical relation (r_1 relation). Similar to MCD-based methods [16], [12], [17], we aim to minimize their discrepancy. Another relation is intra-hypothesis non-identical relation (r_2 relation). Since they are generated by identical regressors, it is expected that they keep closer, so we still minimize their hypothesis discrepancy. The last relation is the interhypothesis non-identical relation (r_3 relation). Since they are generated by different regressors, we enlarge their hypothesis discrepancy. Based on this, we use \mathcal{L}_{inter} to show the discrepancy between two intermediate outputs, H^* from inference branch and H_a^* from adversarial branch:

$$\mathcal{L}_{inter}(x_i^t) = \mathcal{MMD}_{output}(\boldsymbol{H^*}, \boldsymbol{H_a^*}) = L_{r1} + L_{r2} - L_{r3},$$
(6)

$$\begin{cases}
L_{r1} = \frac{1}{K} \sum_{m=1}^{k} \mathcal{MMD}_{keypoint}(h_m^*, h_{a,m}^*) \\
L_{r2} = \frac{1}{K(K-1)} \sum_{m=1}^{k} \sum_{n \neq m} \mathcal{MMD}_{keypoint}(h_m^*, h_n^*) \\
L_{r3} = \frac{1}{K(K-1)} \sum_{m=1}^{k} \sum_{n \neq m} \mathcal{MMD}_{keypoint}(h_m^*, h_{a,n}^*)
\end{cases}$$
(7)

Here * means intermediate, while m and n correspond to different keypoints. L_{r1} is for the inter-hypothesis identical keypoint discrepancy, while L_{r2} is for the intra-hypothesis non-identical discrepancy, and L_{r3} is for the inter-hypothesis non-identical situation. Similarly, we get the discrepancy between specific regressors' outputs as:

$$\mathcal{L}_{spec}(x_i^t) = \mathcal{MMD}_{output}(F'(G(x_i^t)), F_a'(G(x_i^t))). \tag{8}$$

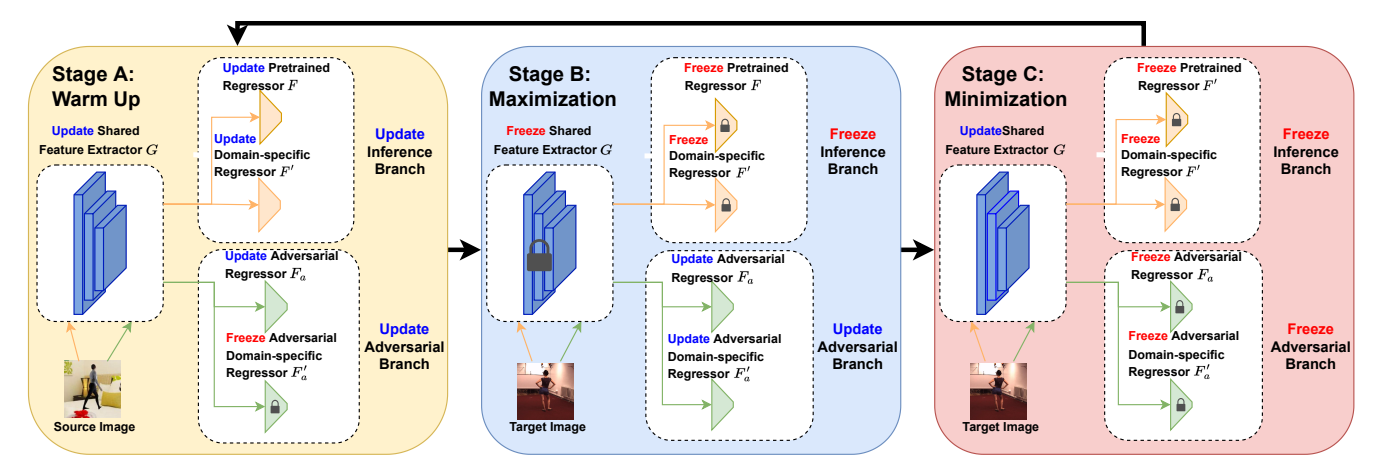


Fig. 6: Overall framework of our method. It includes a shared feature extractor G and two regression branches, the inference branch, and the adversarial branch. Each branch has two regressors, one for general-purpose estimation and the other for domain-specific estimation.

Therefore, with Eq. 6 and Eq. 8, we can compute the proposed hypothesis discrepancy loss in Eq. 3.

E. Overall Objectives and Optimizations

In this part, we summarize one iteration of adversarial adaptation including three stages, as shown in Fig. 6. Stage A is for warm-up, Stage B tries to maximize branch discrepancy, and Stage C aims to minimize branch discrepancy.

Stage A: Warm-up Stage. At this stage, we use source data to warm up two untrained regressors F' and F_a at the beginning, and only F'_a is fixed here. The reason is that we need to use the two regressors in each branch to represent intermediate domains. Since F is well-pretrained, the difference between $F(G(\cdot))$ and $F'(G(\cdot))$ can be maintained. But if we warm up F_a and F'_a simultaneously with identical losses, $F_a(G(\cdot)) - F'_a(G(\cdot))$ will become very close to zero and cannot represent intermediate domain, hence harming the proceeding stages. Furthermore, this step is implemented to mitigate the issue of forgetting on source domain as the number of training epochs increases. The objective can be represented as:

$$\min_{G,F,F',F_{a}} \mathbb{E}_{x_{i}^{s},y_{i}^{s} \in \mathcal{S}} \mathcal{L}_{mse}(F(G(x_{i}^{s})), T^{-1}(y_{i}^{s})) \\
+ \alpha_{1} \mathcal{L}_{mse}(F(G(x_{i}^{s})), F'(G(x_{i}^{s}))) \\
+ \alpha_{2} \mathcal{L}_{mse}(F(G(x_{i}^{s})), F_{a}(G(x_{i}^{s}))).$$
(9)

Stage B: Maximization Stage. At this stage, we start the *max* process of the min-max game. In our proposed IDF, the goal is to maximize the discrepancy between the two branches, which is achieved by enlarging the discrepancy between intermediate representations and reducing the discrepancy between specific representations simultaneously. The shared feature extractor and inference branch are fixed, and only F_a and F'_a from the adversarial branch are updated:

$$\max_{F_a, F_a'} \mathbb{E}_{x_i^t \in \mathcal{T}} \mathcal{L}_{mse}(F(G(x_i^t)), F_a(G(x_i^t))) + \beta \mathcal{L}_{dl}(x_i^t). \tag{10}$$

Without this stage, the outputs from two branches can be very similar and cannot detect target elements outside the support of the source. Stage C: Minimization Stage. For the final stage, we tackle the min process of the min-max game. We hope that the discrepancy between the two branches can be minimized, which is achieved by reducing the discrepancy between intermediate representations and enlarging the discrepancy between specific representations at the same time. In such a case, only G is updated and all the other parts are fixed. The shared feature extractor confuses the two branches and makes them closer:

$$\min_{G} \mathbb{E}_{x_i^t \in \mathcal{T}} \mathcal{L}_{mse}(F(G(x_i^t)), F_a(G(x_i^t))) \\
+ \mathcal{L}_{oks}(T(F(G(x_i^t))), T(F_a(G(x_i^t)))) \\
+ \gamma \mathcal{L}_{dl}(x_i^t).$$
(11)

We still use \mathcal{L}_{mse} and \mathcal{L}_{dl} at this stage but optimize a different objective. This stage encourages target information to be detected with the source support. To address similar concerns about the heatmap errors during the transformation as in the pretraining stage, we add \mathcal{L}_{oks} . We provide PyTorch-like pseudo-code of our method in Supplementary.

IV. EXPERIMENTS

A. Datasets

We use three human-pose datasets and three hand-pose datasets to validate our approach. SURREAL [45] is the source human pose dataset and offers six million synthetic human pose images. Human3.6M [15] is one of the target human pose datasets and is a widely used real-world dataset in the community. It contains 3.6 million images split into 7 folds, and we treat S1, S5, S6, S7, S8 as the training set and S9, S11 as the testing set according to [16] and [19]. **Leeds Sports Pose** [18] (LSP) is the other target human dataset. It is a real-world dataset with 2,000 images and all of them are used for adaptation. Human pose tasks focus on two domain adaptation tasks SURREAL → Human3.6M and SURREAL -> LSP. Rendered Hand Pose Dataset [58] (RHD) is the source hand dataset with 43,986 synthetic hand images. 41,258 of them are used for training and the rest 2,728 are tackled with validation. **Hand-3D-Studio** [53]

(H3D) is one of the two target hand datasets, which includes 22,000 real-world frames. Following the policy from [16] and [19], 18,800 frames are used for training and the others are for testing. **FreiHand** [59] is the other target hand dataset, providing 130k real-world images, and we use all of them for our adaptation task. Hand pose tasks focus on two domain adaptation tasks RHD \rightarrow H3D and RHD \rightarrow FreiHand.

B. Implementation Details

Following previous works [16], [19], Simple Baseline [47] with ResNet-101 [13] is adopted as the HPE backbone. In the *pretrain* process, 70 epochs are conducted, each with 500 iterations. The initial pretrain learning rate is 1e-3 with Adam [20] optimizer. The learning rate drops to 1e-4 at 30 epochs and 1e-5 at 50 epochs. As for the *adaptation* process, 40 epochs are executed with a total of 30,000 iterations. SGD [1] is applied as the optimizer with momentum 0.9 and weight decay 1e-4. The initial learning rate of the shared feature extractor is 1e-3, and that of each regressor is 1e-2. We use the learning rate scheduler with the same strategy used by [16].

Regarding hyperparameters, we set $\alpha_1 = \alpha_2 = 0.5$, and select β as 0.2. Besides, γ is set to be 0.55. To represent the maximization process of Stage B better, we use the same strategy as [16] to minimize negative heatmaps built from spatial probability. All experiments are conducted on Nvidia RTX A5000 GPUs.

C. Main Results

Baselines. Since this paper focuses on *domain adaptive* 2D pose estimation, four recent methods **CC-SSL** [26], **MDAM** [21], **RegDA** [16] and **UniFrame** [19] with SOTA performances are chosen as baselines for comparison. Besides, we add **Source-only** as another baseline for all four tasks to evaluate the effectiveness of adaptation. Since RHD \rightarrow H3D and SURREAL \rightarrow Human3.6M use separate sets for the target domain during training and validation, we add **Oracle** as another baseline, which is jointly trained with target annotations.

Metrics. Percentage of Correct Keypoint (PCK) is adopted as in previous work. We set the ratio of correct prediction as 5% and report PCK@0.05 in Tables I-IV. Apart from overall keypoint accuracy, joints are divided into several part segments and measured by specific metrics following [16], [19]. For the 21-keypoint hand skeleton, MCP, PIP, DIP, and Fin are applied. For the 18-keypoint human skeleton, Sld, Elb, Wrist, Hip, Knee, and Ankle are selected.

Quantitative Results. Table I and Table II are for two hand tasks RHD→H3D and RHD→FreiHand. Our method reaches state-of-the-art for both tasks and achieves a significant lead of 3.4% and 2.8%. Table III and Table IV are for human tasks SURREAL→Human3.6M and SURREAL→LSP. Our model again outperforms all the baselines (except the Oracle) by a considerable margin of 3.2% and 2.8%, respectively. Oualitative Results. Figs. 7 and 8 show qualitative results on

Qualitative Results. Figs. 7 and 8 show qualitative results on H3D and Human3.6M, while Figs. 9 and 10 show qualitative results on FreiHand and LSP. We use Source only, RegDA

TABLE I: PCK@0.05 on RHD \rightarrow H3D Task

Method	MCP	PIP	DIP	Fin	All
Source-only	67.4	64.2	63.3	54.8	61.8
Oracle	97.7	97.2	95.7	92.5	95.8
CC-SSL [26]	81.5	79.9	74.4	64.0	75.1
MDAM [21]	82.3	79.6	72.3	61.5	74.1
RegDA [16]	79.6	74.4	71.2	62.9	72.5
UniFrame [19]	86.7	84.6	78.9	68.1	79.6
Ours	88.9	88.1	82.1	71.9	83.0

TABLE II: PCK@0.05 on RHD → FreiHand Task

Method	MCP	PIP	DIP	Fin	All
Source-only	35.2	50.1	54.8	50.7	46.8
CC-SSL [26]	37.4	48.2	50.1	46.5	43.8
MDAM [21]	32.3	48.1	51.7	47.3	45.1
RegDA [16]	40.9	55.0	58.2	53.1	51.1
UniFrame [19]	43.5	64.0	67.4	62.4	58.5
Ours	46.0	65.2	69.5	63.7	61.3

TABLE III: PCK@0.05 on SURREAL → Human3.6M Task

Method	Sld	Elb	Wrist	Hip	Knee	Ankle	All
Source-only	69.4	75.4	66.4	37.9	77.3	77.7	67.3
Oracle	95.3	91.8	86.9	95.6	94.1	93.6	92.9
CC-SSL [26]	44.3	68.5	55.2	22.2	62.3	57.8	51.7
MDAM [21]	51.7	83.1	68.9	17.7	79.4	76.6	62.9
RegDA [16]	73.3	86.4	72.8	54.8	82.0	84.4	75.6
UniFrame [19]	78.1	89.6	81.1	52.6	85.3	87.1	79.0
Ours	80.8	91.6	82.3	56.0	87.8	88.9	82.2

TABLE IV: PCK@0.05 on SURREAL \rightarrow LSP Task

Method	Sld	Elb	Wrist	Hip	Knee	Ankle	All
Source-only	51.5	65.0	62.9	68.0	68.7	67.4	63.9
CC-SSL [26]	36.8	66.3	63.9	59.6	67.3	70.4	60.7
MDAM [21]	61.4	77.7	75.5	65.8	76.7	78.3	69.2
RegDA [16]	62.7	76.7	71.1	81.0	80.3	75.3	74.6
UniFrame [19]	69.2	84.9	83.3	85.5	84.7	84.3	82.0
Ours	72.1	86.4	85.2	87.7	87.0	86.2	84.8

[16], UniFrame [19], Ours, and Ground Truth (GT) for qualitative comparison. It is evident from these figures that our method provides better adaptation outcomes with more accurate human or hand poses.

D. Ablation Study on Discrepancy Loss

We further conduct a detailed ablation study on the three terms in Eq. 7 using two tasks RHD \rightarrow H3D and SURREAL \rightarrow Human3.6M. According to the three relations described in Section III-D, seven combinations r_1 , r_2 , r_3 , r_1 & r_2 , r_1 & r_3 , r_2 & r_3 , and r_1 & r_2 & r_3 are implemented and the results are listed in Tables V and VI.

TABLE V: Ablation of discrepancy loss terms on RHD \rightarrow H3D task

Method	MCP	PIP	DIP	Fin	All
$\overline{r_1}$	85.5	86.2	80.7	72.0	79.4
r_2	82.1	81.7	76.9	70.1	74.3
r_3	83.7	82.6	77.7	69.5	74.0
$r_1 \& r_2$	88.8	88.0	81.6	72.5	82.2
$r_1 \& r_3$	87.4	87.3	81.1	72.0	80.6
$r_2 \ \& \ r_3$	88.0	87.7	80.6	71.9	80.8
$r_1 \& r_2 \& r_3$	89.6	88.5	82.4	73.0	83.5

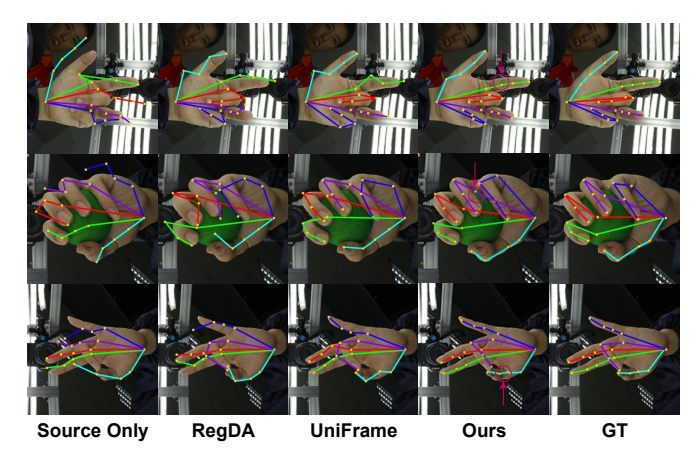


Fig. 7: Qualitative results on H3D dataset

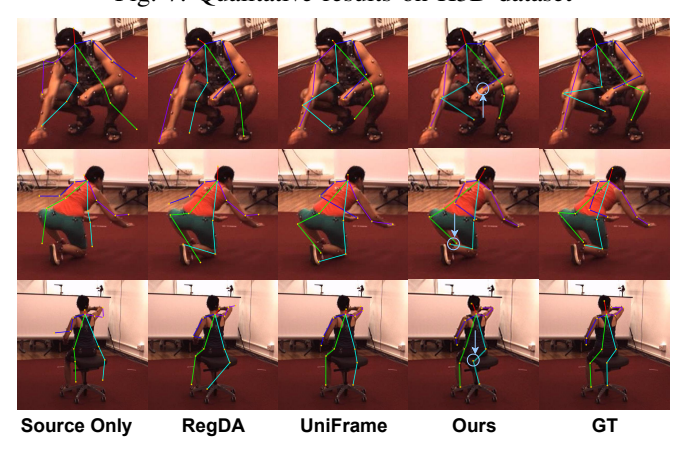


Fig. 8: Qualitative results on Human3.6M dataset

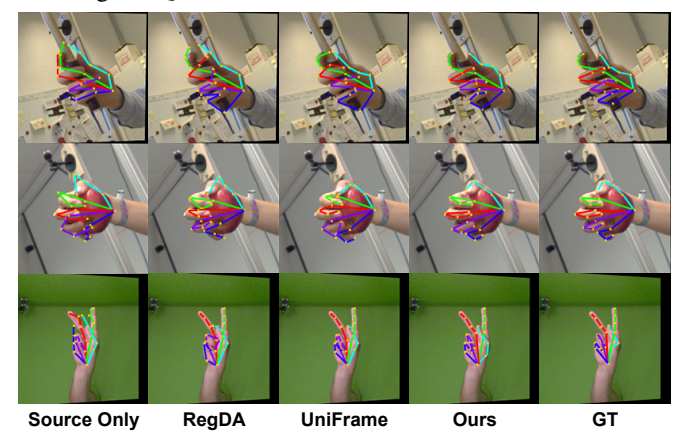


Fig. 9: Qualitative results on FreiHand dataset TABLE VI: Ablation of discrepancy loss terms on SUR-REAL \rightarrow Human3.6M task

Method	Sld	Elb	Wrist	Hip	Knee	Ankle	All
r_1	77.3	91.0	80.4	54.5	84.0	85.8	78.6
r_2	75.7	89.4	79.2	53.0	82.6	83.9	76.8
r_3	76.1	89.8	78.2	52.5	82.5	84.3	77.3
$r_1 \& r_2$	80.6	91.9	81.5	55.7	85.9	87.4	81.6
$r_1 \& r_3$	78.9	91.6	80.3	55.1	83.3	87.0	80.4
$r_2 \& r_3$	78.0	90.9	81.4	54.9	84.3	86.6	79.8
$r_1 \& r_2 \& r_3$	81.5	92.3	82.9	56.4	88.8	89.2	82.7

We observe that all these three relations have an impact on the effectiveness of our proposed discrepancy



Fig. 10: Qualitative results on LSP dataset

loss. Simply considering one relation is not ideal, because even the best situation r_1 still underperforms the baseline UniFrame. On the other hand, the removal of r_1 , r_2 or r_3 will degrade the model's performance. Simply removing r_1 leads to a decrease of 2.7% in RHD \rightarrow H3D and 2.9% in SURREAL \rightarrow Human3.6M. Simply removing r_2 leads to a decrease of 2.9% in RHD \rightarrow H3D and 2.3% in SURREAL \rightarrow Human3.6M. As for r_3 , eliminating it causes a drop of 1.3% in RHD \rightarrow H3D and 1.1% in SURREAL \rightarrow Human3.6M. More results on other tasks are provided in Supplementary.

E. Ablation Study on Network Structures

- 1) Network Structures Comparison: To validate the effectiveness of our proposed Intermediate Domain Framework (IDF), we compare it with the Baseline and an Alternative Intermediate Domain Framework (AIDF). Specifically, 'Baseline' is the conventional structure as shown in Fig. 4 (a). Since there exists only one head in each branch of the Baseline, the domain-specific characteristics persist in both heads, which hinders the aggregation procedure of their outputs. Our proposed 'IDF' (Fig. 4 (b)) solves this issue by adding two explicit specific heads to two branches separately, obtaining two intermediate representations for segregating specific features and aggregate invariant features. A simplified graphical illustration of 'IDF' is also presented in Fig. 11 (a). Unlike our 'IDF', 'AIDF' utilizes two explicit intermediate heads and obtains two specific representations indirectly.
- 2) Variants of Discrepancy: Within each framework, we identify three discrepancy variants that govern the aggregation or segregation of representations from two distinct branches, as depicted in Fig. 11. The variant Inter aims to minimize the discrepancy of intermediate representations, aligning with the aggregation process. The variant Spec seeks to maximize the discrepancy between specific representations, aligning with the segregation process. DL is our proposed discrepancy measure formulated in Eq. 3, which encompasses both Inter and Spec aspects. The influence of these discrepancy variants on each framework is assessed and documented in Tables VII and VIII.

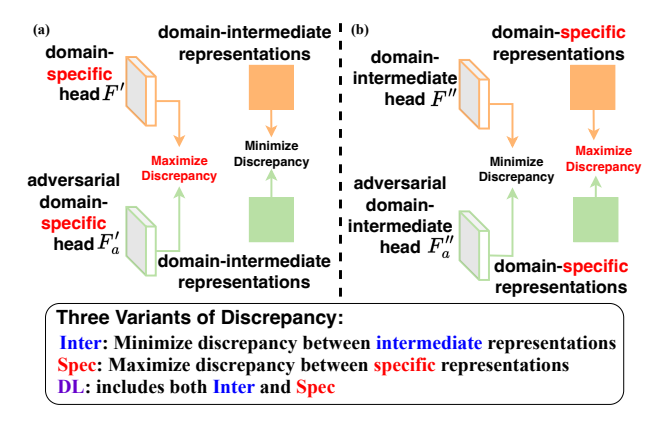


Fig. 11: Comparisons between (a) our proposed Intermediate Domain Framework (IDF), and (b) Alternative Intermediate Domain Framework (AIDF). Detailed illustrations are in **Sec. IV-E**.

Specifically, the terms 'AIDF' and 'IDF' in these tables refer to the utilization of only the inference and adversarial heads, respectively, for each branch (which is similar to the Baseline approach). The term 'Baseline w/ DL' pertains to the reduction of discrepancy between the two heads of the Baseline, as it does not allow for the disentanglement of invariant and specific features.

- 3) Observations: Based on the results in these two tables, we conclude several observations:
 - Adversarial models fail to exhibit enhanced performance by employing 'IDF' or 'AIDF' exclusively, without integrating any discrepancy variants. However, when 'IDF' or 'AIDF' is combined with these variants, there is a significant performance boost. This occurs because when only two heads are used as in the 'Baseline', the network structures do not effectively perform feature disentanglement, rendering them identical to the 'Baseline'.
 - Disentangling invariant and specific representations is necessary, and our 'IDF' is better than 'AIDF' in disentanglement. Notably, in the category of methods using 'w/ DL', 'IDF w/ DL' achieves a performance gain of 3.7% compared to 'Baseline w/ DL' on SURREAL → Human3.6M, and it also outperforms 'AIDF w/ DL' by 2.9%. The substantial improvements achieved by 'AIDF' over the Baseline underscore the critical importance of disentangling invariant and specific representations within heads for improved adaptation. And the noticeable disparity between IDF's performance and that of 'AIDF' suggests that the construction of explicit specific heads is a more effective approach compared to AIDF's method of employing explicit intermediate heads. This distinction arises from the neural network's inherent capability to more easily extract specific features as opposed to invariant features.
 - Solely adopting 'Inter' or 'Spec' results in limited performance improvement. However, when these two components cooperate and form 'DL', the performances show significant improvement. Specifically, on the RHD → H3D task, applying only 'Inter' to 'IDF' leads to an increase of 2.3%, and using only 'IDF w/ Spec' results

in an improvement of 1.7%. In contrast, when 'DL' is formed, the performance boost becomes substantial at 8.2%. The results show that the process of learning invariant representations relies on both aggregating domain-invariant features and segregating domain-specific features, and these two processes can help each other get better.

TABLE VII: Ablation study on RHD \rightarrow H3D task

Method	MCP	PIP	DIP	Fin	All
Baseline	82.2	75.9	72.6	63.0	74.5
Baseline w/ DL	83.0	77.6	74.7	65.5	75.9
AIDF	82.2	76.1	73.0	63.5	74.6
AIDF w/ Inter	83.3	76.9	73.7	64.2	75.4
AIDF w/ Spec	82.6	76.5	73.6	63.8	74.9
AIDF w/ DL	84.7	79.9	75.3	67.0	77.8
IDF	82.3	76.1	73.4	64.2	74.8
IDF w/ Inter	85.5	78.3	75.2	66.1	77.1
IDF w/ Spec	84.9	78.1	74.6	65.8	76.5
IDF w/ DL (Ours)	88.9	88.1	82.1	71.9	83.0

 $\underline{TABLE\ VIII:\ Ablation\ study\ on\ SURREAL\rightarrow Human 3.6M}$

Method	Sld	Elb	Wrist	Hip	Knee	Ankle	All
Baseline	74.5	88.0	72.4	54.6	84.0	85.0	77.7
Baseline w/ DL	76.0	90.8	75.1	55.2	84.4	86.4	78.5
AIDF	74.7	88.8	74.7	54.5	84.2	85.3	77.7
AIDF w/ Inter	75.6	89.3	75.4	55.0	84.6	86.0	78.8
AIDF w/ Spec	75.3	88.8	75.3	54.7	84.0	85.9	78.1
AIDF w/ DL	78.4	91.1	76.5	55.2	85.9	86.6	79.3
IDF	74.7	89.5	75.0	54.8	84.3	85.7	77.8
IDF w/ Inter	76.4	91.0	77.9	55.3	85.6	87.2	80.7
IDF w/ Spec	75.5	90.7	77.3	55.0	86.2	86.8	80.3
IDF w/ DL (Ours)	80.8	91.6	82.3	56.0	87.8	88.9	82.2

F. Analysis of Training Efficiency

To assess the training efficiency in a fair manner, we conducted experiments using the RHD

H3D task on a single Nvidia RTX A5000 GPU. By comparing the training times of RegDA, UniFrame, and our method, as presented in Table IX, we observe that ours takes similar time as RegDA (while achieving significant improvements over RegDA), but considerably less time than UniFrame. This discrepancy in training times underscores the efficacy of our method in achieving superior performance while maintaining competitive training durations. Specifically, our method exhibits a balance between training efficiency and performance gains, making it a compelling choice for real-world applications where computational resources and time constraints are critical factors to consider. Moreover, the notable reduction in training time compared to UniFrame highlights the potential scalability and feasibility of our approach for large-scale deployment and practical usage scenarios.

TABLE IX: Comparisons of Training Time

	RegDA	UniFrame	Ours
Style Transfer Time	0	7h45min	0
Pretrain Epoch/Time	70/3h05min	70/3h10min	70/3h07min
Adaptation Epoch/Time	60/4h12min	60/6h10min	60/5h23min
All Time	7h17min	17h05min	8h29min
Performance (PCK@0.05)	72.5	79.6	83.0

V. CONCLUSION

In this paper, we propose a novel domain adaptive pose estimation model, where we aim to alleviate the transfer difficulty via disentangling features into domain-intermediate and domain-specific components, along with aggregation and segregation of them separately. Moreover, we design a new discrepancy measurement that exploits various keypoint relationships and apply separate aggregation or segregation strategies to them. Extensive experiments are conducted on hand and human pose datasets, showing that our approach outperforms the state-of-the-art methods by significant mar-

REFERENCES

- [1] S.-i. Amari. Backpropagation and stochastic gradient descent method.
- Neurocomputing, 5(4-5):185–196, 1993.
 [2] S. Ben-David, J. Blitzer, K. Crammer, A. Kulesza, F. Pereira, and J. W. Vaughan. A theory of learning from different domains. Machine learning, 79:151-175, 2010.
- [3] Y. Chen, Z. Wang, Y. Peng, Z. Zhang, G. Yu, and J. Sun. Cascaded pyramid network for multi-person pose estimation. In Proceedings of the IEEE Conference on Computer Vision and Pattern Recognition,
- pages 7103–7112, Salt Lake City, Utah, 2018. IEEE. [4] J. Deng, W. Dong, R. Socher, L.-J. Li, K. Li, and L. Fei-Fei. Imagenet: A large-scale hierarchical image database. In 2009 IEEE conference on computer vision and pattern recognition, pages 248-255, Miami, Florida, 2009. IEEE.
- W. Deng, Q. Liao, L. Zhao, D. Guo, G. Kuang, D. Hu, and L. Liu. Joint clustering and discriminative feature alignment for unsupervised domain adaptation. IEEE Transactions on Image Processing: a Publication of the IEEE Signal Processing Society, 30:7842-7855, 2021
- [6] A. Dosovitskiy, L. Beyer, A. Kolesnikov, D. Weissenborn, X. Zhai, T. Unterthiner, M. Dehghani, M. Minderer, G. Heigold, S. Gelly, J. Uszkoreit, and N. Houlsby. An image is worth 16x16 words: Transformers for image recognition at scale. In International Conference on Learning Representations, page N/A, Vienna, Austria, 2021. Open Review
- [7] Y. Ganin and V. Lempitsky. Unsupervised domain adaptation by backpropagation. In International Conference on Machine Learning, ages 1180-1189, Lille, France, 2015. PMLR.
- I. Goodfellow, J. Pouget-Abadie, M. Mirza, B. Xu, D. Warde-Farley, S. Ozair, A. Courville, and Y. Bengio. Generative adversarial networks. Communications of the ACM, 63(11):139-144, 2020.
- [9] A. Gretton, K. M. Borgwardt, M. J. Rasch, B. Schölkopf, and A. Smola. A kernel two-sample test. The Journal of Machine Learning Research, 13(1):723-773, 2012.
- [10] S. Gu, Y. Feng, and Q. Liu. Improving domain adaptation translation with domain invariant and specific information. In Proceedings of the 2019 Conference of the North American Chapter of the Association for Computational Linguistics: Human Language Technologies, Volume 1 (Long and Short Papers), pages 3081-3091, Minneapolis, Minnesota, 2019. NAACL
- [11] R. Hadsell, S. Chopra, and Y. LeCun. Dimensionality reduction by learning an invariant mapping. In 2006 IEEE computer society conference on computer vision and pattern recognition (CVPR'06), volume 2, pages 1735–1742, New York City, New York, 2006. IEEE. [12] Z. Han, H. Sun, and Y. Yin. Learning transferable parameters
- for unsupervised domain adaptation. IEEE Transactions on Image Processing, 31:6424-6439, 2022.
- [13] K. He, X. Zhang, S. Ren, and J. Sun. Deep residual learning for image recognition. In Proceedings of the IEEE Conference on Computer Vision and Pattern Recognition, pages 770-778, Las Vegas, Nevada, 2016. IEEE.
- [14] X. Huang and S. Belongie. Arbitrary style transfer in real-time with adaptive instance normalization. In Proceedings of the IEEE International Conference on Computer Vision, pages 1501-1510, Venice, Italy, 2017, IEEE,
- [15] C. Jonescu, D. Papava, V. Olaru, and C. Sminchisescu. Human3. 6m: Large scale datasets and predictive methods for 3d human sensing in natural environments. IEEE Transactions on Pattern Analysis and Machine Intelligence, 36(7):1325–1339, 2013. [16] J. Jiang, Y. Ji, X. Wang, Y. Liu, J. Wang, and M. Long. Regressive
- domain adaptation for unsupervised keypoint detection. In Proceedings of the IEEE/CVF Conference on Computer Vision and Pattern Recognition, pages 6780-6789, Nashville, Tennessee, 2021. IEEE.

- [17] R. Jin, J. Zhang, J. Yang, and D. Tao. Multibranch adversarial regression for domain adaptative hand pose estimation. IEEE Transactions on Circuits and Systems for Video Technology, 32(9):6125-6136, 2022.
- S. Johnson and M. Everingham. Clustered pose and nonlinear appearance models for human pose estimation. In British Machine Vision Conference, volume 2, page 5, Britain, 2010. Citeseer, BMVC.
- [19] D. Kim, K. Wang, K. Saenko, M. Betke, and S. Sclaroff. A unified framework for domain adaptive pose estimation. In European Conference on Computer Vision, pages 603-620, Switzerland, 2022. Springer.
- [20] D. Kingma, L. Ba, et al. Adam: A method for stochastic optimization. 2015.
- [21] C. Li and G. H. Lee. From synthetic to real: Unsupervised domain adaptation for animal pose estimation. In Proceedings of the IEEE/CVF Conference on Computer Vision and Pattern Recognition,
- pages 1482–1491, Nashville, Tennessee, 2021. IEEE. [22] K. Li, S. Wang, X. Zhang, Y. Xu, W. Xu, and Z. Tu. Pose recognition with cascade transformers. In Proceedings of the IEEE/CVF Conference on Computer Vision and Pattern Recognition, pages 1944-1953, Nashville, Tennessee, 2021. IEEE.
- T.-Y. Lin, M. Maire, S. Belongie, J. Hays, P. Perona, D. Ramanan, P. Dollár, and C. L. Zitnick. Microsoft coco: Common objects in context. In European Conference on Computer Vision, pages 740-755, Zurich, Switzerland, 2014. Springer.
- [24] M. Long, Y. Cao, J. Wang, and M. Jordan. Learning transferable features with deep adaptation networks. In International Conference on Machine Learning, pages 97-105, Lille, France, 2015. PMLR.
- Z. Luo, Z. Wang, Y. Huang, L. Wang, T. Tan, and E. Zhou. Rethinking the heatmap regression for bottom-up human pose estimation. In Proceedings of the IEEE/CVF Conference on Computer Vision and Pattern Recognition, pages 13264–13273, Nashville, Tennessee, 2021.
- [26] J. Mu, W. Qiu, G. D. Hager, and A. L. Yuille. Learning from synthetic animals. In Proceedings of the IEEE/CVF Conference on Computer Vision and Pattern Recognition, pages 12386-12395, Seattle, Washington, 2020. IEEE.
- Q. Peng. Multi-source and source-private cross-domain learning for visual recognition. Master's thesis, Purdue University, 2022.
- [28] Q. Peng, Z. Ding, L. Lyu, L. Sun, and C. Chen. Rain: regularization on input and network for black-box domain adaptation. In Proceedings of the Thirty-Second International Joint Conference on Artificial Intelligence, pages 4118-4126, Macau, China, 2023. IJCAI.
- Q. Peng, B. Planche, Z. Gao, M. Zheng, A. Choudhuri, T. Chen, C. Chen, and Z. Wu. 3d vision-language gaussian splatting. arXiv preprint arXiv:2410.07577, 2024.
- [30] Q. Peng, C. Zheng, and C. Chen. Source-free domain adaptive human pose estimation. In Proceedings of the IEEE/CVF International Conference on Computer Vision, pages 4826-4836, Paris, France, 2023 IEEE
- [31] Q. Peng, C. Zheng, and C. Chen. A dual-augmentor framework for domain generalization in 3d human pose estimation. In Proceedings of the IEEE/CVF Conference on Computer Vision and Pattern Recognition, pages 2240-2249, 2024.
- [32] E. Pinyoanuntapong, A. Ali, K. Jakkala, P. Wang, M. Lee, Q. Peng, C. Chen, and Z. Sun. Gaitsada: Self-aligned domain adaptation for mmwave gait recognition. In 2023 IEEE 20th International Conference on Mobile Ad Hoc and Smart Systems (MASS), pages 218-226. IEEE. 2023.
- [33] D. S. Raychaudhuri, C.-K. Ta, A. Dutta, R. Lal, and A. K. Roy-Chowdhury. Prior-guided source-free domain adaptation for human pose estimation. In Proceedings of the IEEE/CVF International Conference on Computer Vision, pages 14996-15006, Vancouver, Canada, 2023. IEEE.
- K. Saito, K. Watanabe, Y. Ushiku, and T. Harada. Maximum classifier discrepancy for unsupervised domain adaptation. In Proceedings of the IEEE Conference on Computer Vision and Pattern Recognition.
- pages 3723–3732, Salt Lake City, Utah, 2018. IEEE.
 [35] D. Shi, X. Wei, L. Li, Y. Ren, and W. Tan. End-to-end multiperson pose estimation with transformers. In *Proceedings of the* IEEE/CVF Conference on Computer Vision and Pattern Recognition, pages 11069-11078, New Orleans, Louisiana, 2022. IEEE.
- [36] P. Stojanov, Z. Li, M. Gong, R. Cai, J. Carbonell, and K. Zhang. Domain adaptation with invariant representation learning: What transformations to learn? Advances in Neural Information Processing Systems, 34:24791-24803, 2021.
- B. Sun and K. Saenko. Deep coral: Correlation alignment for deep domain adaptation. In European Conference on Computer Vision,

- pages 443–450, Amsterdam, Netherlands, 2016. Springer. [38] K. Sun, B. Xiao, D. Liu, and J. Wang. Deep high-resolution representation learning for human pose estimation. In Proceedings of the IEEE/CVF Conference on Computer Vision and Pattern Recognition, pages 5693–5703, Long Beach, California, 2019. IEEE. [39] X. Sun, J. Shang, S. Liang, and Y. Wei. Compositional human pose
- regression. In Proceedings of the IEEE International Conference on Computer Vision, pages 2602–2611, Venice, Italy, 2017. IEEE. [40] X. Sun, B. Xiao, F. Wei, S. Liang, and Y. Wei. Integral human pose
- regression. In Proceedings of the European Conference on Computer Vision (ECCV), pages 529-545, Munich, Germany, 2018. Springer.
- [41] H. Tang, K. Chen, and K. Jia. Unsupervised domain adaptation via structurally regularized deep clustering. In Proceedings of the IEEE/CVF Conference on Computer Vision and Pattern Recognition, pages 8725-8735, Seattle, Washington, 2020. IEEE.
- [42] A. Tarvainen and H. Valpola. Mean teachers are better role models: Weight-averaged consistency targets improve semi-supervised deep learning results. Advances in Neural Information Processing Systems, 30:1195-1204, 2017.
- [43] A. Toshev and C. Szegedy. Deeppose: Human pose estimation via deep neural networks. In Proceedings of the IEEE Conference on Computer Vision and Pattern Recognition, pages 1653-1660, Columbus, Ohio, 2014. IEEE
- [44] E. Tzeng, J. Hoffman, N. Zhang, K. Saenko, and T. Darrell. Deep domain confusion: Maximizing for domain invariance. arXiv preprint arXiv:1412.3474, 2014.
- [45] G. Varol, J. Romero, X. Martin, N. Mahmood, M. J. Black, I. Laptev, and C. Schmid. Learning from synthetic humans. In Proceedings of the IEEE Conference on Computer Vision and Pattern Recognition, pages 109–117, Honolulu, Hawaii, 2017. CVPR.
- [46] H. Wu, H. Zhu, Y. Yan, J. Wu, Y. Zhang, and M. K. Ng. Heterogeneous domain adaptation by information capturing and distribution matching. IEEE Transactions on Image Processing, 30:6364-6376, 2021.
- [47] B. Xiao, H. Wu, and Y. Wei. Simple baselines for human pose estimation and tracking. In Proceedings of the European Conference on Computer Vision (ECCV), pages 466-481, Munich, Germany, 2018.
- [48] Y. Xin, J. Du, Q. Wang, Z. Lin, and K. Yan. Vmt-adapter: Parameterefficient transfer learning for multi-task dense scene understanding. In Proceedings of the AAAI Conference on Artificial Intelligence,
- volume 38, pages 16085–16093, 2024. [49] Y. Xin, J. Du, Q. Wang, K. Yan, and S. Ding. Mmap: Multi-modal alignment prompt for cross-domain multi-task learning. In Proceedings of the AAAI Conference on Artificial Intelligence, volume 38,
- pages 16076–16084, 2024. [50] Y. Xin, S. Luo, X. Liu, Y. Du, H. Zhou, X. Cheng, C. L. Lee, J. Du, H. Wang, M. Chen, et al. V-petl bench: A unified visual parameterefficient transfer learning benchmark. In The Thirty-eight Conference on Neural Information Processing Systems Datasets and Benchmarks
- [51] R. Xu, G. Li, J. Yang, and L. Lin. Larger norm more transferable: An adaptive feature norm approach for unsupervised domain adaptation. In Proceedings of the IEEE/CVF International Conference on Computer Vision, pages 1426-1435, Seoul, South Korea, 2019. IEEE.
- [52] F. Zhang, X. Zhu, H. Dai, M. Ye, and C. Zhu. Distribution-aware coordinate representation for human pose estimation. In Proceedings of the IEEE/CVF Conference on Computer Vision and Pattern Recognition.
- pages 7093–7102, Seattle, Washington, 2020. IEEE. [53] Z. Zhao, T. Wang, S. Xia, and Y. Wang. Hand-3d-studio: A new multiview system for 3d hand reconstruction. In ICASSP 2020-2020 IEEE International Conference on Acoustics, Speech and Signal Processing
- (ICASSP), pages 2478–2482, Barcelona, Spain, 2020. IEEE. [54] C. Zheng, M. Mendieta, T. Yang, G.-J. Qi, and C. Chen. Feater: An efficient network for human reconstruction via feature mapbased transformer. In Proceedings of the IEEE/CVF Conference on Computer Vision and Pattern Recognition, 2023.
- [55] C. Zheng, S. Zhu, M. Mendieta, T. Yang, C. Chen, and Z. Ding. 3d human pose estimation with spatial and temporal transformers. In Proceedings of the IEEE/CVF international conference on computer vision, pages 11656-11665, 2021.
- [56] Y. Zhu, F. Zhuang, and D. Wang. Aligning domain-specific distribution and classifier for cross-domain classification from multiple sources. In Proceedings of the AAAI Conference on Artificial Intelligence,
- volume 33, pages 5989–5996, 2019. [57] F. Zhuang, Z. Qi, K. Duan, D. Xi, Y. Zhu, H. Zhu, H. Xiong, and Q. He. A comprehensive survey on transfer learning. Proceedings of the IEEE, 109(1):43–76, 2020.
 [58] C. Zimmermann and T. Brox. Learning to estimate 3d hand pose

- from single rgb images. In Proceedings of the IEEE International Conference on Computer Vision, pages 4903-4911, Honolulu, Hawaii,
- Zimmermann, D. Ceylan, J. Yang, B. Russell, M. Argus, and T. Brox. Freihand: A dataset for markerless capture of hand pose and shape from single rgb images. In Proceedings of the IEEE/CVF International Conference on Computer Vision, pages 813-822, Long Beach, California, 2019. IEEE.

VI. SUPPLEMENTARY MATERIAL OVERVIEW

The supplementary material is organized into the following sections:

- Section VII: Parameter sensitivity analysis.
- Section VIII: Additional ablation study on FreiHand and LSP datasets.
- Section IX: Additional ablation of discrepancy loss terms on FreiHand and LSP datasets.
- Section X: Ablation of varied loss functions to measure discrepancy.
- Section XI: Domain generalization to unseen domains based on models trained on domain adaptation tasks.
- Section XII: Qualitative results on the unseen dataset COCO based on models trained on domain adaptation tasks

VII. PARAMETER SENSITIVITY ANALYSIS

We use RHD \rightarrow H3D and SURREAL \rightarrow Human3.6M to illustrate the sensitivity of α_1 and α_2 , β , and γ in the main paper. Since the terms associated with α_1 and α_2 are very similar (in order to warm up two heads), we integrate them into α . Fig. 12 and Fig. 13 exhibit the results under different parameter settings. From it, we observe that the decreases from different parameters are limited to 0.12% for α , β , and γ . Therefore, our method shows stable performance over hyperparameters.

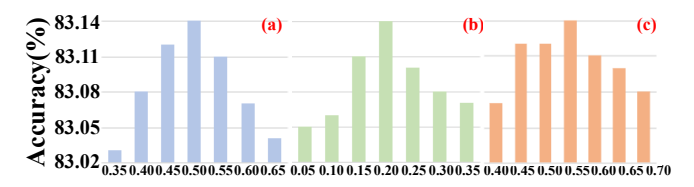


Fig. 12: Parameter Analysis on RHD \rightarrow H3D (best viewed in color). **a**: Analysis on α . **b**: Analysis on β . **c**: Analysis on γ .

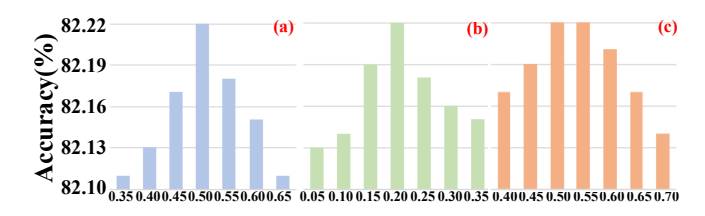


Fig. 13: Analysis on SURREAL \rightarrow Human3.6M (best viewed in color). **a**: Analysis on α . **b**: Analysis on β . **c**: Analysis on γ .

VIII. ADDITIONAL ABLATION STUDY

In this section, we provide additional ablation study on the two tasks RHD→FreiHand and the SURREAL→LSP, and the results are shown in Table X and Table XI. There are three components **Intermediate Domain Framework** (**IDF**), **Discrepancy Loss** (**DL**), and **Reweighting** (**RW**). On the RHD → FreiHand task, applying only 'Inter' to 'IDF' leads to an increase of 4.0%, and using only 'IDF w/

Spec' results in an improvement of 3.2%. In contrast, when 'DL' is formed, the performance boost becomes substantial at 9.6%. The results show that the process of learning invariant representations relies on both aggregating domain-invariant features and segregating domain-specific features, and these two processes can help each other get better.

TABLE X: Ablation Study on RHD → FreiHand Task

MCP	PIP	DIP	Fin	All
40.3	55.8	57.9	52.9	50.6
41.1	57.6	58.5	54.0	53.4
40.5	55.6	57.8	53.0	50.6
41.7	56.8	59.9	54.4	52.1
41.1	55.9	58.6	54.0	51.7
43.6	58.1	60.9	58.2	55.4
40.4	55.5	57.9	53.2	50.7
42.8	60.4	62.5	56.9	54.7
42.4	58.5	59.7	55.1	53.9
46.0	65.2	69.5	63.7	61.3
	40.3 41.1 40.5 41.7 41.1 43.6 40.4 42.8 42.4	40.3 55.8 41.1 57.6 40.5 55.6 41.7 56.8 41.1 55.9 43.6 58.1 40.4 55.5 42.8 60.4 42.4 58.5	40.3 55.8 57.9 41.1 57.6 58.5 40.5 55.6 57.8 41.7 56.8 59.9 41.1 55.9 58.6 43.6 58.1 60.9 40.4 55.5 57.9 42.8 60.4 62.5 42.4 58.5 59.7	40.3 55.8 57.9 52.9 41.1 57.6 58.5 54.0 40.5 55.6 57.8 53.0 41.7 56.8 59.9 54.4 41.1 55.9 58.6 54.0 43.6 58.1 60.9 58.2 40.4 55.5 57.9 53.2 42.8 60.4 62.5 56.9 42.4 58.5 59.7 55.1

TABLE XI: Ablation Study on SURREAL \rightarrow LSP Task

Method	Sld	Elb	Wrist	Hip	Knee	Ankle	All
Baseline	62.8	77.0	71.3	81.4	80.5	75.6	74.9
Baseline w/ DL	64.0	77.7	72.5	82.0	81.6	77.1	76.5
AIDF	63.2	77.1	71.5	81.0	80.6	75.4	74.8
AIDF w/ Inter	64.1	78.2	73.3	82.4	82.2	77.6	76.9
AIDF w/ Spec	63.4	77.5	72.0	81.7	81.4	76.0	75.5
AIDF w/ DL	66.6	80.8	75.4	84.2	83.0	80.9	81.1
IDF	62.9	77.2	71.7	81.4	80.5	75.9	74.9
IDF w/ Inter	65.9	80.8	74.0	84.1	83.3	81.6	80.6
IDF w/ Spec	64.4	79.3	73.5	82.8	82.0	79.7	78.3
IDF w/ DL (Ours)	72.1	86.4	85.2	87.7	87.0	86.2	84.8

IX. Additional Ablation of Discrepancy Loss Terms

In this section, we present additional ablation of discrepancy loss terms on the RHD \rightarrow FreiHand task and the SURREAL \rightarrow LSP task, and the results are listed in Table XII and Table XIII. As described in the main manuscript, three terms r_1 , r_2 , and r_3 are considered in the proposed method. It is noticeable that r_2 plays a more important role than r_3 , since the removal of r_2 leads to a decrease of 3.6% in RHD \rightarrow FreiHand and 2.7% in SURREAL \rightarrow LSP, while that of r_3 results in a reduction of 1.7% in RHD \rightarrow FreiHand and 1.5% in SURREAL \rightarrow LSP.

TABLE XII: Ablation of discrepancy loss terms on RHD \rightarrow FreiHand Task

Method	MCP	PIP	DIP	Fin	All
$\overline{r_1}$	41.6	62.7	65.8	60.2	56.9
r_2	40.9	61.1	64.0	59.7	55.2
r_3	40.4	61.3	64.4	60.9	57.8
$r_1 \& r_2$	44.1	65.3	68.7	62.1	59.0
$r_1 \& r_3$	42.6	64.6	68.3	61.5	57.7
$r_2 \& r_3$	43.5	64.9	68.9	61.8	58.6
$r_1 \& r_2 \& r_3$	46.0	65.2	69.5	63.7	61.3

TABLE XIII: Ablation of discrepancy loss terms on SUR-REAL \rightarrow LSP Task

Method	Sld	Elb	Wrist	Hip	Knee	Ankle	All
r_1	67.9	82.2	81.8	84.7	84.3	80.1	80.6
r_2	65.3	80.7	80.0	82.5	81.6	78.8	78.2
r_3	66.4	81.3	80.9	83.7	82.2	79.0	78.8
$r_1 \& r_2$	71.0	85.0	83.3	84.1	85.5	84.7	83.2
$r_1 \& r_3$	70.6	83.8	81.3	82.6	84.8	83.7	81.9
$r_2 \& r_3$	70.7	84.3	81.9	83.5	85.4	84.2	82.5
$r_1 \& r_2 \& r_3$	72.1	86.4	85.2	87.7	87.0	86.2	84.8

X. ABLATION OF VARIED LOSS FUNCTIONS

In our proposed method, MMD loss [56] is applied to measure discrepancy. Unlike KL divergence, which measures the distance between two distributions, and MSE loss, which gauges the spatial difference between two heatmaps, the MMD loss is a specific metric crafted for assessing the distance between two hypotheses [56], [9]. **This is particularly relevant to our proposed multi-branch (multi-hypotheses) framework.** Furthermore, we substitute the MMD loss in \mathcal{L}_{dl} with KL divergence and MSE loss for empirical comparisons. The results are presented in Tab. XIV, showing the superiority of MMD over MSE and KL Divergence.

TABLE XIV: Ablation of loss functions on RHD \rightarrow H3D task

Method	MCP	PIP	DIP	Fin	All
MSE	82.7	75.9	71.0	62.2	73.5
KL Divergence	83.3	80.4	75.7	63.9	77.8
MMD (Ours)	89.6	88.5	82.4	73.0	83.5

XI. GENERALIZATION TO UNSEEN DOMAINS

Following prior works [21], [19], we also conduct experiments on the generalization to unseen domains. For hand pose estimation, we use models adapted in the RHD \rightarrow H3D task and evaluate their performances on the validation set of FreiHand, as shown in Table XV. For human pose estimation, we use models adapted in the SURREAL \rightarrow LSP task and evaluate their performance on Human3.6M, as shown in Table XVI.

TABLE XV: Domain Generalization on FreiHand

Method	MCP	PIP	DIP	Fin	All
Source-only	34.9	48.7	52.4	48.5	45.8
Oracle	92.8	90.3	87.7	78.5	87.2
CC-SSL [26]	34.3	46.3	48.4	44.4	42.6
MDAM [21]	29.6	46.6	50.0	45.3	42.2
RegDA [16]	37.8	51.8	53.2	47.5	46.9
UniFrame [19]	35.6	52.3	55.4	50.6	47.1
Ours	38.0	52.5	54.8	50.6	47.4

From these two tables, we can see that our model still outperforms other approaches for a lead of 0.3% on FreiHand and 0.4% on Human3.6M, which is not as large as that of the adaptation tasks presented in the main paper. This is partly

TABLE XVI: Domain Generalization on Human3.6M

Method	Sld	Elb	Wrist	Hip	Knee	Ankle	All
Source-only	51.5	65.0	62.9	68.0	68.7	67.4	63.9
Oracle	95.3	91.8	86.9	95.6	94.1	93.6	92.9
CC-SSL [26]	52.7	76.9	63.1	31.6	75.7	72.9	62.2
MDAM [21]	54.4	75.3	62.1	21.6	70.4	69.2	58.8
RegDA [16]	76.9	80.2	69.7	52.0	80.3	80.0	73.2
UniFrame [19]	77.0	85.9	73.8	47.6	80.7	80.6	74.3
Ours	77.5	82.9	74.1	53.3	80.2	80.8	74.7

because our model is designed for adaptation problems, not for generalization settings specifically. Nevertheless, our method still achieves the best results in these generalization experiments as compared to the state-of-the-art, demonstrating its superiority.

XII. QUALITATIVE RESULTS ON THE UNSEEN DATASET COCO

In this section, we present qualitative visualizations on the COCO dataset [23], which was not included in our previous human dataset studies due to differences in annotation methods. While we cannot provide quantitative generalization results due to these discrepancies, we believe that our qualitative results are still meaningful. To conduct our analysis, we utilized the model trained on the SURREAL → LSP task in combination with the pre-trained SURREAL model, and the resulting visualizations are shown in Fig. 14. These results demonstrate that our model is capable of generalizing to an unseen dataset, suggesting that the adaptation process has a positive impact on the model's generalization ability.



Fig. 14: Qualitative results on the COCO dataset. Here we compare our method trained from SURREAL \rightarrow LSP with the source-only model.